

Pure rotational spectra of TiO and TiO₂ in VY Canis Majoris[★]

T. Kamiński¹, C. A. Gottlieb², K. M. Menten¹, N. A. Patel², K. H. Young²,
S. Brünken³, H. S. P. Müller³, M. C. McCarthy², J. M. Winters⁴, L. Decin^{5,6}

¹ Max-Planck Institut für Radioastronomie, Auf dem Hügel 69, 53121 Bonn, Germany,
e-mail: kaminski@mpi.fr.de

² Harvard-Smithsonian Center for Astrophysics, 60 Garden Street, Cambridge, MA, USA

³ I. Physikalisches Institut, Zùlpicher Strasse 77, 50937 Köln, Germany

⁴ Institut de Radioastronomie Millimétrique, 300 rue de la Piscine, 38406 Saint-Martin d'Hères, France

⁵ Instituut voor Sterrenkunde, Katholieke Universiteit Leuven, Celestijnenlaan 200D, 3001 Leuven, Belgium

⁶ Sterrenkundig Instituut Anton Pannekoek, University of Amsterdam, Science Park 904, 1098 Amsterdam, The Netherlands

Received; accepted

ABSTRACT

We report the first detection of pure rotational transitions of TiO and TiO₂ at (sub-)millimeter wavelengths towards the red supergiant VY CMa. A rotational temperature, T_{rot} , of about 250 K was derived for TiO₂. Although T_{rot} was not well constrained for TiO, it is likely somewhat higher than that of TiO₂. The detection of the Ti oxides confirms that they are formed in the circumstellar envelopes of cool oxygen-rich stars and may be the “seeds” of inorganic-dust formation, but alternative explanations for our observation of TiO and TiO₂ in the cooler regions of the envelope cannot be ruled out at this time. The observations suggest that a significant fraction of the oxides is not converted to dust, but instead remains in the gas phase throughout the outflow.

Key words. Astrochemistry; Stars: winds, outflows; Circumstellar matter, Stars: individual: VY CMa; Line: identification

1. Introduction

Copious amounts of dust, omnipresent in cool circumstellar environments, are produced by stars at the final stages of their evolution, yet the formation of dust by depletion of molecules from the gas phase is poorly understood. In low-mass stars, the formation of dust is thought to be most efficient in the asymptotic giant branch (AGB), and in massive stars during the red supergiant phase. There are two major types of dust produced by cool stars. Carbon stars (e.g., C-type AGB stars and RCrB stars), which have more carbon than oxygen in their circumstellar environments, produce mainly carbon dust which nucleates from abundant aromatic hydrocarbons (Sedlmayr & Dominik 1995, and references therein). In oxygen-rich circumstellar envelopes (e.g., M-type AGB stars and red supergiants), essentially all carbon is locked into CO and the dust is inorganic. How such inorganic grains start to form remains elusive. After ruling out species containing the more abundant elements (Si, Fe, and Mg) and taking into account infrared (IR) observations of circumstellar dust shells in cool oxygen-rich giants and supergiants, Gail & Sedlmayr (1998) concluded on the basis of a chemical equilibrium model that the formation of inorganic dust at higher temperatures entails molecules containing less abundant elements. Gail & Sedlmayr showed that at temperatures expected at the onset of dust formation, ~1200K, the refractory molecules TiO and TiO₂ are the first species in the chain of reactions that produce titanium oxide clusters which are the “seeds”

needed to initiate further dust formation at temperatures below the condensation temperature of TiO (see also Jeong et al. 2003).

Prior to this work, TiO₂ had not been identified in an astrophysical object either at optical or radio wavelengths, but TiO has been observed at visible wavelengths in M-type stars for many decades (Merrill et al. 1962, and references therein). The electronic bands of TiO are so prominent in late-type stars, that the Morgan-Keenan spectroscopic classification is based in part on the relative strengths of these bands (Morgan & Keenan 1973). However, the electronic bands in these studies are *photospheric* absorption features, which do not provide any insight into the warm circumstellar chemistry. Occasionally the optical bands of TiO are observed in emission from the warm circumstellar gas, but such cases are extremely rare and difficult to interpret (Barnbaum et al. 1996; Kamiński et al. 2010). Perhaps the most extreme example of the importance of TiO as an opacity source in oxygen-rich stars at optical wavelengths are high-amplitude mira variables, for which molecular absorption of TiO may be responsible for the variation of optical light by up to 8 mag (Reid & Goldston 2002).

Radio astronomers had long sought TiO in the interstellar medium and circumstellar environments (Churchwell et al. 1980; Millar et al. 1987; Brünken et al. 2008), because observations of its rotational lines might yield the temperature and abundances more directly than at optical wavelengths. Although there have been several attempts to observe TiO at radio wavelengths (most with single antennas), all were unsuccessful. In the past few years it was realized that images obtained with sensitive interferometers with sub-arcsecond resolution might have

Send offprint requests to: T. Kamiński

[★] Based on observations carried out with the Submillimeter Array, IRAM Plateau de Bure Interferometer, and data acquired within the ESO program 67.B-0504.

sufficient sensitivity to observe the pure rotational spectrum of TiO and possibly TiO₂.

The rotational spectrum of TiO was measured in the laboratory many years ago (Namiki et al. 1988), and the essential laboratory spectroscopic measurements needed to identify TiO₂ at optical and radio wavelengths were reported more recently. The rotational spectrum of TiO₂ was first observed in the laboratory when Brünken et al. (2008) measured 13 transitions to high accuracy in the centimeter band. Brünken et al. determined the rotational and leading centrifugal distortion constants that allow predictions of the astronomically important transitions in the millimeter and submillimeter bands which subsequent measurements confirmed are accurate to 0.5 km s⁻¹ or better (Kania et al. 2011). Unfortunately, the prospect for identifying TiO₂ at optical wavelengths appears difficult, because the most promising band at ~5300 Å may be obscured by a more intense band of TiO.

The red supergiant VY CMa appeared to be the best source to search for TiO and TiO₂ at (sub-)millimeter wavelengths, because optical emission bands of refractory oxides including ScO, YO, VO, and TiO have long been known to be present in this extreme star;¹ and the (sub-)millimeter spectrum of VY CMa is unusually rich for an oxygen-rich source. In recent spectral line surveys at millimeter wavelengths at the Arizona Radio Observatory (e.g., Ziurys et al. 2007; Tenenbaum et al. 2010), the number of detected molecules in VY CMa increased to 21 including metal oxides (e.g., AlO and PO) and other exotic molecules (e.g., AlOH and PN). Some of the newly discovered molecules are refractory species important for dust formation in oxygen-rich CSEs.

In 2010, we made a wide band line survey of VY CMa in the 345-GHz band with the Submillimeter Array (SMA). Present in this survey are rotational lines of both TiO and TiO₂. The identifications of TiO and TiO₂ were confirmed in 2012 by independent measurements with the IRAM Plateau de Bure Interferometer (PdBI) of lines within the 220.7–224.3 GHz range. In Sect. 2, we briefly describe the SMA and PdBI observations; in Sect. 3, the line identification and properties of the TiO and TiO₂ emission are presented; in Sect. 4, the rotational-temperature diagrams for both molecules are analyzed; in Sect. 5, the (sub-)millimeter TiO emission is compared with optical observations of this molecule; and finally, in the Sect. 6, the observed properties of the emission are discussed within the broad context of inorganic dust formation.

2. Observations

Rotational lines of the two simplest Ti oxides (TiO and TiO₂) were detected in a 345 GHz-band spectral line survey with the SMA². The results of the survey together with a detailed description of the observations and data reduction will be described elsewhere. Here we provide a brief description of the observations.

The spectral line survey of VY CMa covers the entire frequency range between 279.1 and 355.1 GHz, except for very narrow 32 MHz wide gaps at every 2 GHz interval. The observations were done between 17 January and 2 February 2010. The typical time spent in each 4 GHz wide band was about 3.9 h, and

¹ Approximate luminosity (scaled to a distance of 1.2 kpc, Zhang et al. 2012) is $3 \cdot 10^5 L_{\odot}$, effective temperature $T_{\text{eff}}=3200\text{--}3500$ K, and radius $R_{\star}=1500\text{--}3000 R_{\odot}$ (see Appendix in Humphreys et al. 2007; Wittkowski et al. 2012).

² The raw survey data are available at <http://www.cfa.harvard.edu/cgi-bin/sma/smaarch.pl>

the rms noise for spectra extracted with an aperture of 1'' was about 70 mJy per resolution element of 0.7 km s⁻¹. The noise is fairly uniform over the entire range of the survey except for the region between 321–327 GHz, owing to a strong telluric absorption band of water.

The SMA was used in its extended configuration to produce a synthesized beam with a full width at half-maximum (FWHM) of about 0''.9. The phase center was at $\alpha(2000)=07^{\text{h}}22^{\text{m}}58.332^{\text{s}}$, $\delta(2000)=-25^{\circ}46'03.17''$. All necessary calibrations (gain, flux, bandpass) were secured during the observations. The data were calibrated in the MIR-IDL package³. After a careful inspection of the flux calibration, we estimate that its typical uncertainty is about 15%. The continuum map of VY CMa (0.6 Jy) was used to self-calibrate the data in phase and to correct for some of the phase variations. Most of the further data processing, including map production from calibrated visibilities, was performed in Miriad (Sault et al. 1995).

To confirm our identification of TiO and TiO₂ with the SMA, we made an independent observation of a 3.6 GHz-wide band near 222.45 GHz with the PdBI on 22 April and 13 October 2012. The frequency range (220.65–224.25 GHz) was chosen so as to maximize the number of unblended and relatively strong lines of TiO and TiO₂ which could be observed simultaneously in the 1.35 mm band. The PdBI was used in the D configuration with six antennas. Owing to the low declination of VY CMa, the maximum elevation is only 19°. As a result, the observations were affected by antenna shadowing and the synthesized beam is very asymmetric (4''.9×2''.2, with a position angle of the major axis of 158°). The observations of VY CMa were interleaved every 22 min by short integrations on nearby phase and amplitude calibrators (first 0648-165 and 0646-306, then switching to 0648-165 and 0823-223 when the elevation of 0646-306 was too low). Pointing and focus were checked about every 65 min. The observations were made with the dual-polarization single-sideband receiver (tuned in the lower side band) and the WideX correlator, which provides a resolution of 2 MHz (corresponding to 2.7 km s⁻¹ at the observing frequency). The data were calibrated using the GILDAS⁴ software package and the final processing included self-calibration in phase on the strong continuum of VY CMa. The thermal noise in the combined data set is ~8 mJy/beam per 2.7 km s⁻¹ bin.

3. Line identification and measurements

In all, 220 spectral lines were observed in the SMA survey. Initially we were able to assign all except about 30 on the basis of the close coincidence between the astronomical frequency and laboratory rest frequencies (ν_{rest}) tabulated in the standard catalogs (Cologne Database for Molecular Spectroscopy, CDMS, Müller et al. 2005, 2001; Jet Propulsion Laboratory Catalogue, Pickett et al. 1998). Of the remaining unassigned features, lines of TiO were relatively easy to recognize in the spectrum because they were narrower than most others, while TiO₂ was one of the last species considered in our iterative identification procedure.

The full spectrum obtained with PdBI is shown and described in Appendix A. All of the lines of TiO and TiO₂ predicted to be present in the spectrum are detected in these very sensitive observations.

Below, we describe the identification and present the spectra of TiO and TiO₂. Data from the SMA survey are presented first and are followed by a description of the PdBI data, as this is the

³ <http://cfa-www.harvard.edu/~cgi/mircook.html>

⁴ <http://www.iram.fr/IRAMFR/GILDAS>

chronological order that influenced the analysis. A search for isotopologues in all the available data is described in Sect. 3.5. Some constraints on the emission angular sizes and position are given in Sect. 3.6. The evidence in support of the identifications is summarized in Sect 3.7.

3.1. TiO in the SMA survey

The TiO radical has a X³Δ electronic ground state that is split into three fine structure components with energies relative to the lowest ³Δ₁ component of 140 K (³Δ₂) and 280 K (³Δ₃). The rotational spectrum of TiO had been measured to high accuracy in the laboratory by Namiki et al. (1988) and the dipole moment was measured recently ($\mu=3.34$ D; Steimle & Virgo 2003). Starting with the $J=3\rightarrow 2$ transition, roughly every 32 GHz there is a rotational transition ($J'\rightarrow J$) separated by 3–4 GHz from the corresponding transition in the next lower or higher fine structure component. Eight transitions of TiO were covered in the survey: all three components in $J=9\rightarrow 8$ and $10\rightarrow 9$, but only two components were covered in $J=11\rightarrow 10$ because the third (at 355.6 GHz) lies slightly outside the upper end of the observed range.

Six lines of TiO were detected above the 3σ level in the SMA survey. Maps of the integrated emission, confirm that all six lines are from a source centered (within uncertainties) on the star (see Sect. 3.6). Of the two missing transitions, the line at 291.0 GHz is located close to a gap and the baseline in the region near the line is uncertain. If the baseline in this spectrum is removed in a least squares fit with a polynomial, the edge of the spectrum near the gap is slightly lower and the fluxes in the frequency range of the expected feature of TiO are greater than 3 times the local rms noise. However, in the following discussion we treat the line at 291.0 GHz as though it had not been detected, and the measurements cited here are for the spectrum with a linear baseline subtracted (see below). The line at 323.3 GHz ($J=10\rightarrow 9$ in ³Δ₃) is located in the frequency region affected by the absorption band of terrestrial water and the noise is much greater than the expected intensity. As a result, none of the lines of the ³Δ₃ component was definitely detected.

The most intense line of TiO at 348.2 GHz may be blended with very weak emission from a line of ³⁴SO₂ at 348.117 GHz. Approximately 30 lines of SO₂ were observed in the survey, and from these a rotational temperature of 85 ± 10 K was derived. On the assumption that T_{rot} is the same for ³⁴SO₂, we estimate that the contribution from the possibly interfering line of ³⁴SO₂ is <5% of the measured fluxes of TiO. We cannot rule out *a priori* that the lines of TiO (and those of TiO₂, see Sect. 3.3) might be blended with species whose carriers have not been identified in the survey, nor can we exclude entirely the possibility of blends with weak lines from species that have been identified. However the contribution to the measured fluxes from the latter should not be significant, because of the small aperture used in our analysis ($1''\times 1''$). For example, in a molecule like SO₂, which has intense broad lines throughout the entire spectrum, the emission is greatest for larger apertures and transitions between the lowest rotational energy levels (cf. Fu et al. 2012).

Listed in Table 1 are the transitions of TiO which were covered with SMA and PdBI, their peak and integrated fluxes, the rms of the noise in the region near the lines, and the detection levels (signal-to-noise ratios, S/N). The latter are expressed as the integrated flux density, I , divided by the uncertainty, ΔI , resulting from the 1 rms noise level, i.e., $\Delta I = \text{rms} \cdot \Delta V_{\text{ch}} \cdot \sqrt{n_{\text{ch}}}$, where ΔV_{ch} is the channel width for which the rms is specified and n_{ch} is the number of channels within the integrated inter-

Table 1. Observed parameters of the TiO lines.

Transition ^a $J' \rightarrow J, \Omega$	ν_{rest} (GHz)	E_u (K)	S_{ul} ^b	Peak ^c (mJy)	Flux ^d (Jy km s ⁻¹)	rms ^e (mJy)	S/N ^f
PdBI							
7→6, 1	221.580	41	13.71	74	1.2	5.4	26.3
7→6, 2	224.139	181	12.85	73	1.3	7.3	20.5
SMA							
9→8, 1	284.875	67	17.77	150	1.8	46	8.5
9→8, 2	288.156	207	17.11	240	2.3	66	7.6
9→8, 3	290.998	354	16.00	<160	<0.7	50	<3.0
10→9, 1	316.519	82	19.80	230	2.4	50	10.6
10→9, 2	320.159	222	19.20	580	3.1	174	3.9
10→9, 3	323.314	369	18.20	<1470	<14.0	1021	<3.0
11→10, 1	348.160	99	21.81	440	4.7	73	14.1
11→10, 2	352.158	239	21.27	290	2.3	125	4.1

Notes. ^(a) $\Omega = 1, 2, 3$ refers to the fine structure components ³Δ₁, ³Δ₂, or ³Δ₃. ^(b) The quantum mechanical line strength of the rotational transition. ^(c) Peak flux density at a resolution of 2.7 km s⁻¹ (PdBI) or 0.8 km s⁻¹ (SMA) for the full synthesized beam. ^(d) Flux integrated between 6 and 32 km s⁻¹ and within the full synthesized beam. ^(e) The rms per bin of 2.7 km s⁻¹ (PdBI) or 0.8 km s⁻¹ (SMA). ^(f) The signal-to-noise ratio.

val. For those transitions that were not detected, the 3σ upper limit on the fluxes is indicated. Spectra of the individual lines are shown in Fig. 1, while Fig. 2 shows a combined profile of the lines that were detected with SMA, excluding the blended line at 348.16 GHz. The combined spectrum is an average of individual spectra weighted by the rms⁻² and scaled by the reciprocal of the integrated flux.

The line profile of TiO as seen in the SMA combined spectrum alone, extends over the range from about 3 to ≥ 55 km s⁻¹ (Fig. 2). Most of the emission occurs between ~ 3 and ~ 32 km s⁻¹ and is well reproduced by a Gaussian profile centered at $V_{\text{LSR}} = 20 \pm 2$ km s⁻¹ and with a FWHM = 18 ± 2 km s⁻¹. In addition, there is emission that forms a wing that is extended to the red of the main component. The redshifted emission is not discernible in the spectra of individual lines of TiO observed with SMA (Fig. 1).

3.2. TiO in the PdBI data

Two lines of TiO were covered by the PdBI observation are both well detected: the $J=7\rightarrow 6$ transition in the ³Δ₁ and ³Δ₂ spin components at 221.6 GHz and 224.1 GHz. The red wing of the 221.6 GHz line may be very weakly contaminated by TiO₂ emission (see below) and the blue wing of the 224.1 GHz line may be affected by vibrationally excited SO₂ (unlikely; see Appendix A). The spectra of all TiO lines are shown in Fig. 1 and their parameters are listed in Table 1. The line at 221.6 GHz appears more triangular in shape than that at 224.1 GHz, possibly owing to the much different excitation energies of 41 and 181 K.

The average line profile of the PdBI lines is compared to the combined SMA profile in Fig. 2. The PdBI profile is slightly broader than that observed with SMA. In the more sensitive PdBI observations, not only the existence of the red wing is confirmed but also a blue wing is apparent. They form a broad “pedestal” extending from -15 km s⁻¹ to 65 km s⁻¹ (with an uncertainty of about 5 km s⁻¹ in each of the limits). Because the ratio of the central, Gaussian-like component to the broad pedestal is smaller in the PdBI data, the main component appears broader.

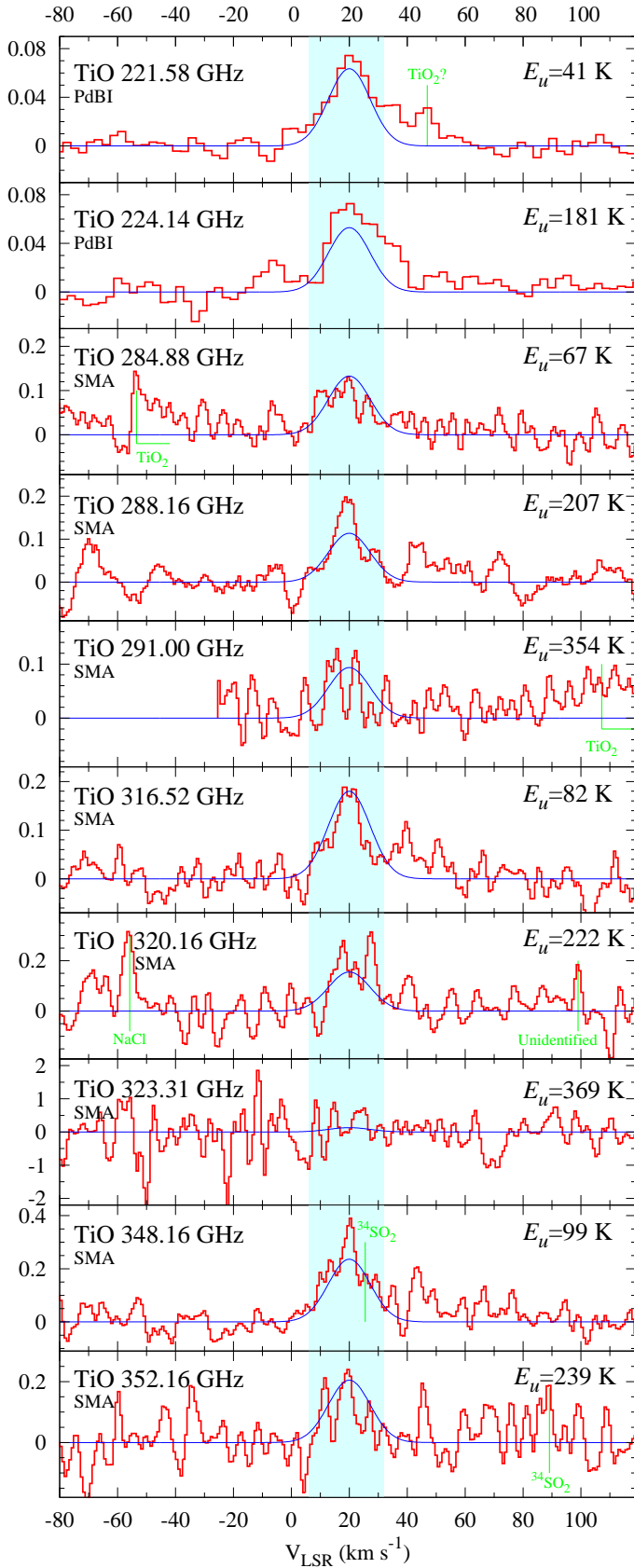


Fig. 1. Spectra of all transitions of TiO covered in the SMA survey and the PdBI spectrum. The shaded area is the range over which the spectra were integrated. Overlaid on the measured spectra are theoretical Gaussian profiles (in blue) plotted on the assumption of LTE at 1000 K. The ordinate is flux density in Jy. Spectra correspond to the aperture of $1'' \times 1''$ (SMA data) or to the full PdBI beam of $4.9'' \times 2.2''$ (PdBI data). The SMA spectra were Hanning smoothed.

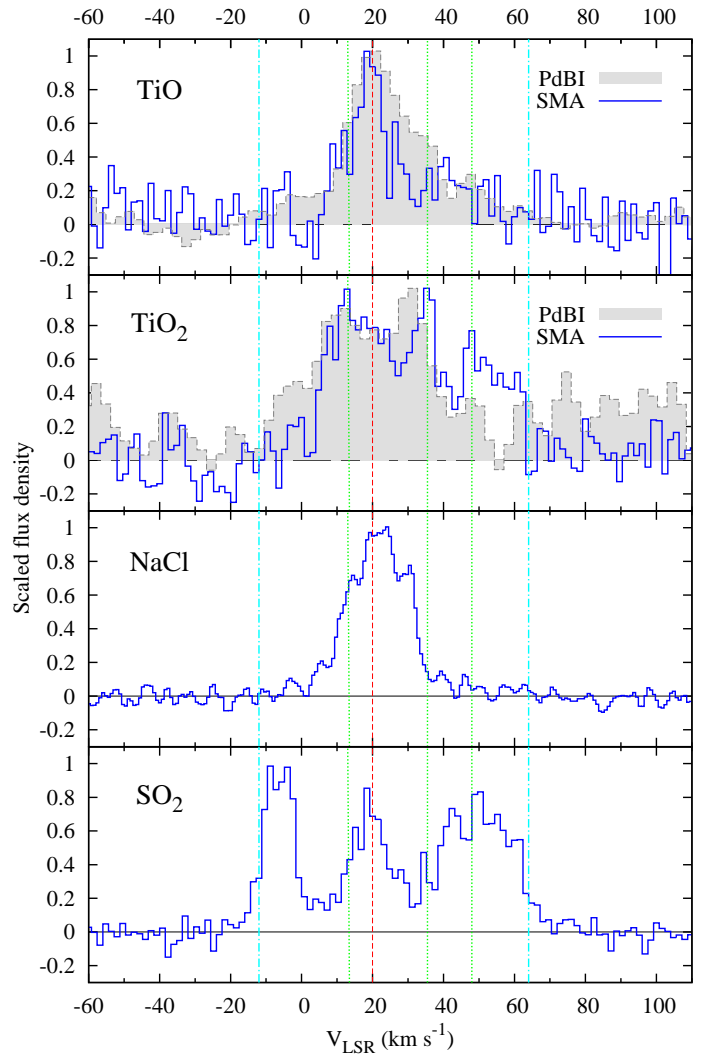


Fig. 2. Two top panels: Spectra of TiO and TiO₂ obtained by combining several lines from the SMA survey (blue line) or PdBI observations (filled grey histogram). They are compared to a combined profile of NaCl emission (third panel) and a strong line of SO₂ ($16_{0,16} \rightarrow 15_{1,15}$) from the SMA survey (bottom panel). Spectra were smoothed and the peak flux density of each was normalized to 1.0. The dashed (red) vertical line marks the line center of TiO at $V_{\text{LSR}}=20 \text{ km s}^{-1}$, and the dotted (green) vertical lines mark 14, 35.5, and 48.0 km s^{-1} identified as peaks of velocity components in the SMA combined profile of TiO₂. The outermost dash-dotted lines (cyan) show the full velocity range of the TiO₂ emission.

3.3. TiO₂ in the SMA data

Titanium dioxide, TiO₂, is an asymmetric top with C_{2v} symmetry and a substantial dipole moment along the b inertial axis ($\mu_b=6.33 \text{ D}$; Wang et al. 2009). Owing to the two equivalent off-axis ¹⁶O bosons, half of the rotational levels are missing. Because it is a fairly heavy molecule, many transitions lie within the range of the survey. We found 20 unblended lines and three pairs of lines that form tight blends of TiO₂ emission. The blend at 337.2 GHz is the most intense feature of TiO₂ in the survey and one that provided the first indication that we may have detected this elusive molecule. In the blends at 331.2 and 337.2 GHz, the flux from each line in the blended pair is nearly the same, because both arise from levels at nearly the same energy above ground and the line strengths are comparable.

Table 2 lists the transitions detected, their flux, and the rms noise. It also contains the uncertainties of the rest frequencies, which typically are below 0.1 MHz, but in a few cases are larger than 1 MHz. Shown in Fig. 3 are the features with the highest S/N, including the blended features at 331.2 and 337.2 GHz. Four unblended lines with the highest S/N (at 285.9, 347.8, 350.4, and 350.7 GHz) were combined to yield an average profile by the same procedure as that for TiO (Fig. 2). The line profile of TiO₂ is broad, with most features extending over the velocity range from about 0 to 62 km s⁻¹. The strong blend at 337.2 GHz suggests, however, that the range may extend as far as -15 km s⁻¹. At least three velocity components at about 14, 35.5, and 48.0 km s⁻¹ are apparent in the combined spectrum.

3.4. TiO₂ in the PdBI data

The Cologne Database for Molecular Spectroscopy lists eight lines of TiO₂ in the frequency range covered by the PdBI observations. They are marked in Fig. A.1, where the length of the markers indicates the relative line intensities expected under local thermodynamic equilibrium (LTE) conditions at 300 K, which is approximately the gas rotational temperature derived from the survey data (Sect. 4). Four are present in the observed spectrum. The one at 221.1 GHz is blended with emission of ³⁴SO₂, which we estimate is weaker than the ³⁴SO₂ line at 221.7 GHz; therefore, the feature at 221.1 GHz is dominated by TiO₂ emission. Two other lines, at 221.41 and 221.45 GHz (i.e., 70 km s⁻¹ apart) overlap slightly; and another two, at 220.9 and 223.5 GHz, are not detected, but are localized in spectral regions free of emission and sensitive upper limits on their emission can be derived. The remaining lines, at 221.55 and 222.96 GHz, are expected to have peak intensities much below the rms noise and coincide with emission lines of TiO and SO₂. The four detected lines are included in Table 2, and the unblended ones are shown in Fig. 3. The integrated flux of the 221.1 GHz line includes the contribution of the ³⁴SO₂ emission and therefore is given as an upper limit in Table 2.

When the PdBI line profiles are compared to each other (Fig. 3), the 220.8 GHz line is centrally peaked at 30 km s⁻¹, while the other two lines are dominated by blue-shifted components peaking between 5 and 10 km s⁻¹. The profiles of the two latter lines are very similar. They have larger-than-average uncertainty in their rest frequencies and a relative shift of the order of one spectral channel (~2.7 km s⁻¹) cannot be excluded. The emission in these two lines can be traced to at least -12 km s⁻¹, which when combined with the positive velocity components observed in some of the SMA lines gives the full velocity range of TiO₂ emission between -12 and 62 km s⁻¹ – see the comparison of the combined profiles⁵ in Fig. 2. The PdBI data confirm that the broad emission of TiO₂ consists of several emission components that have different intensity ratios in individual transitions, suggesting that the components are characterized by a range of excitation temperatures. There is some correspondence (although not exact) in the positions of the main components seen in both combined profiles, e.g., both are dominated by the central double (U-shaped) peak. The PdBI spectra and measurements of TiO and TiO₂ provided in Tables 1 and 2 and Figs. 1 and 3 correspond to the full synthesized beam.

⁵ In the average PdBI profile, some emission outside the -12 → 62 km s⁻¹ range is seen, because the two averaged lines are not well separated in velocity.

3.5. Isotopologues

We did not observe lines of the rare isotopologues of TiO or TiO₂. Because the S/N of the main isotopic species is <26, non-detection of the rare isotopologues is consistent with the standard (solar and meteoritic) elemental composition in which the main isotope ⁴⁸Ti is at least 9 times more abundant than all other isotopes of Ti.

3.6. SMA spatial constraints on the TiO and TiO₂ emission

Maps of integrated emission of TiO and TiO₂ are shown in Figs. 4 and 5. They are compared to maps of continuum emission at 351±2 GHz, and that of NaCl $J=26\rightarrow 25$ and H₂O $v_2 = 2 J_{K_a, K_c} = 5_{2,3} \rightarrow 6_{1,6}$, which are both expected to be compact sources (Milam et al. 2007; Menten et al. 2006). The center of the continuum emission is marked by a white cross in the figures.

We measured the position and sizes of the TiO and TiO₂ emission by performing fits of a two-dimensional (elliptical) Gaussian to the emitting regions. If the synthesized beam is approximated by a Gaussian, then a deconvolved sizes of the emission can be calculated from the fits. For this purpose, we used an automated procedure *imfit* in Miriad. We found that for some TiO transitions the main emission component (between 10 and 30 km s⁻¹) is a point source, i.e., its intrinsic size is much smaller than the beam. For a broader integration interval (6–32 km s⁻¹), the average deconvolved size is 0'5 FWHM. This value has however a large uncertainty owing to the very low S/N of the lines. For the TiO₂ emission analyzed within 0–62 km s⁻¹, the average (weighted by the uncertainty of the Gaussian fit) deconvolved size is 0'6±0'1 FWHM, in agreement with FWHM=0'5±0'1 derived separately for the 337.2 GHz feature alone, which has the highest S/N among all the lines analyzed.

Although the position of the emission for each individual TiO and TiO₂ feature usually agrees to within the (large) errors with the central position of the continuum source, in the case of the TiO line at 316.5 GHz, the measured center is displaced by -0'2 in RA or 5 times the formal error of the fit; similarly, the strong TiO₂ emission at 337. GHz is displaced by -0'2 in RA or 4 times the error. The error-weighted mean values of the TiO and TiO₂ positions for all the analyzed features have a similar offset with respect to the continuum source: ($\Delta\alpha$, $\Delta\delta$)=(-0'15±0'06, 0'12±0'08) for TiO and (-0'20±0'05, 0'08±0'03) for TiO₂, where the 3 σ errors are indicated. The shift appears to be real and is distinguishable in Figs. 4 and 5. A similar offset is measured for other relatively compact molecular emission, e.g., that of vibrationally excited H₂O (see also NaCl; Fig. 5). The nature of the offset is discussed in Sect. 6.1.

The SMA measurements in Tables 1 and 2, and spectra in Figs. 1–3 are for data extracted with a square aperture of 1''×1'' centered on the continuum peak. With the above constraints on the emission size and position, this aperture encloses more than 95% of the emission thereby minimizing the contribution of noise in the spectra. We repeated the entire data analysis procedure including the possible shift in the extraction and obtained essentially the same results as those here. The PdBI measurements and spectra, correspond to the large synthesized beam of 4'9×2'2, and therefore do not provide additional constraints on the size of the emission.

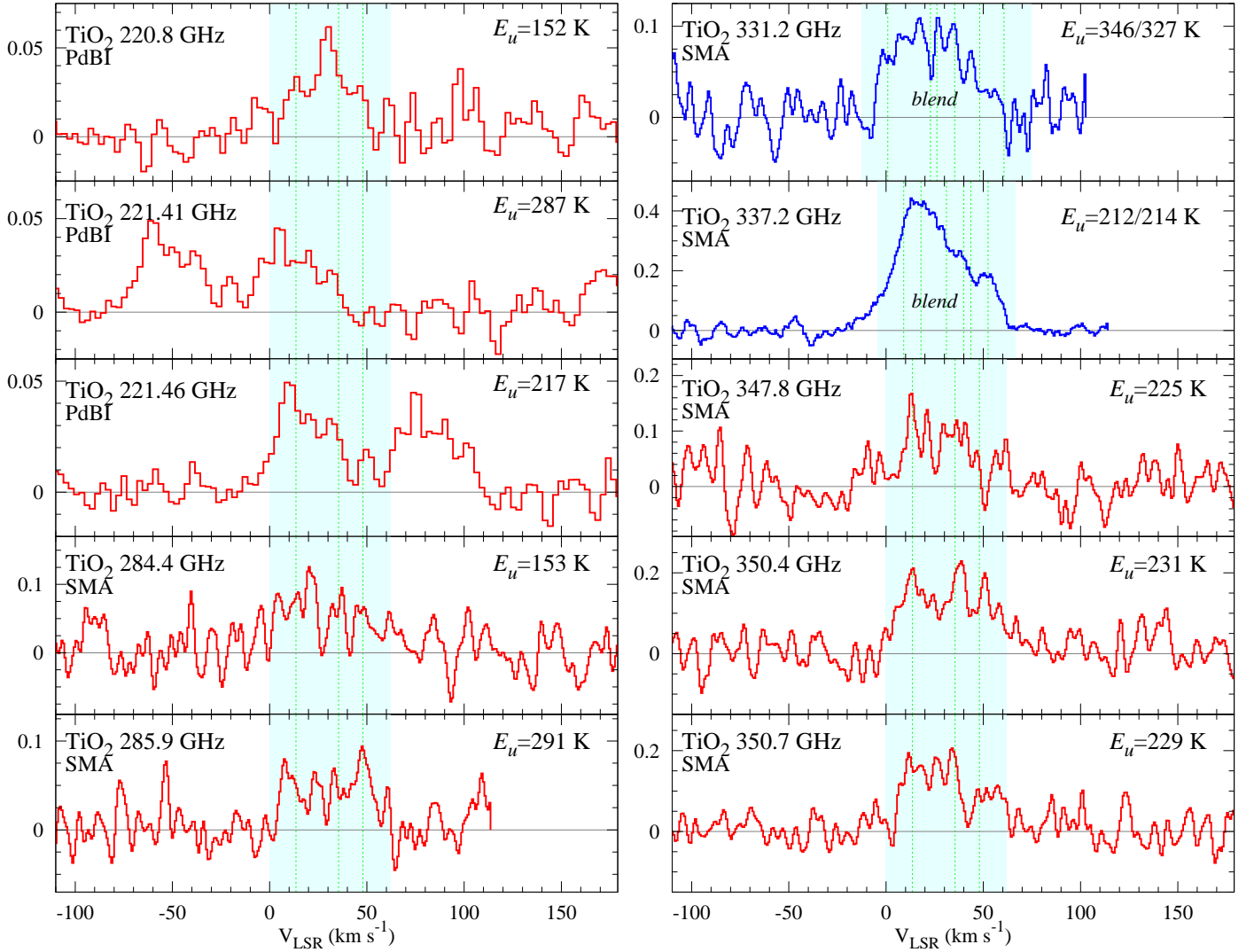


Fig. 3. Spectra of unblended lines of TiO_2 with the the highest S/N, and two blended lines (blue). The velocity scales of the blended lines refer to the average rest frequency of the two components. Parts of the spectra that contain strong emission from other species were blanked for clarity. The lines found in the PdBI observations are shown in the top three panels on the left. The dotted (green) vertical lines mark the position of the three main components of the TiO_2 emission identified in the combined profile (cf. Fig. 2). The ordinate is flux density in Jy and corresponds to the aperture of $1'' \times 1''$ in the SMA spectra or to the full beam size ($4''.9 \times 2''.2$) in the PdBI data. The SMA spectra were Hanning smoothed.

3.7. Summary of evidence in support of the identification of TiO and TiO_2

The evidence that we have observed pure rotational lines of TiO and TiO_2 in VY CMa is overwhelming. Following the initial identification of both molecules in the SMA survey, two new lines of TiO and four of TiO_2 were observed at the predicted intensities in a blind observation with PdBI. The agreement of the astronomical frequencies (V_{LSR}) with laboratory measured frequencies, which are accurate to a small fraction of the line width, is excellent. There are no missing lines for either molecule, nor are there any lines that are anomalously intense. As shown in Fig. 1, the intensities of the eight lines of TiO between 221.58 and 352.16 GHz that were detected and the two upper limits (at 291.00 and 323.31 GHz), agree to within the measurement uncertainties with those derived from a simple LTE analysis (see Sect. 4). For TiO_2 , approximately 20 unblended lines in the SMA survey with intensities within a factor of a few of the most intense lines at 350.4 and 350.7 GHz, are present as predicted (Table 2). Maps of the integrated emission of TiO in Fig. 4 confirm that all six lines observed with SMA are from a compact

source (approximately) centered on the star, with an angular size that is much smaller than our $0''.9$ synthesized beam, as expected for a species predicted to be localized in the inner outflow. As the sample maps in Fig. 5 show, the emission from TiO_2 is similarly compact as that of TiO , and those of NaCl and vibrationally excited H_2O which were observed with the SMA under the same conditions and configuration as that of TiO and TiO_2 .

Circumstantial evidence consistent with the identification of these two titanium oxides is provided by the line profiles, and an estimate of the likelihood of a misassignment owing to interfering background lines. Despite the fairly low S/N, the profile shapes of all the lines assigned to TiO and TiO_2 are consistent (Figs. 1 and 3). Those of TiO are narrow and centrally peaked, while lines of TiO_2 are broad and typically asymmetric with multiple velocity components. Our confidence in the identification is further enhanced by the very low density of lines in our 77 GHz wide survey of approximately 1 line every 380 MHz. The average separation between lines in VY CMa is equivalent to about 25 linewidths of TiO , or 5 linewidths of TiO_2 — i.e., there is very little of the overlapping of features that frequently occurs in

Table 2. Parameters of detected TiO₂ lines.

Transition $J'_{K'_a, K'_c} \rightarrow J_{K_a, K_c}$	$\nu_{\text{rest}}^{\text{a}}$ (MHz)	E_u (K)	S_{ul}	Flux ^b (Jy km s ⁻¹)	rms ^c (mJy)	S/N ^d
PdBI						
23 _{5,19} → 23 _{4,20}	220812.1 (0.2)	230	12.857	1.48	11.0	10.4
4 _{4,0} → 3 _{3,1}	221095.7 (0.0)	25	3.476	<1.77	8.3	16.5
32 _{5,27} → 32 _{4,28}	221406.6 (0.5)	424	19.365	0.91	7.5	9.4
28 _{4,24} → 28 _{3,25}	221458.4 (0.3)	323	14.873	1.45	7.5	14.9
SMA						
10 _{3,7} → 9 _{2,8}	282196.8 (0.0)	50	2.489	1.08	46.1	3.3
21 _{1,21} → 20 _{0,20}	284371.9 (0.1)	153	19.115	3.51	49.5	10.1
20 _{2,18} → 19 _{3,17}	284951.3 (0.0)	161	9.737	2.25	47.2	6.8
25 _{7,19} → 25 _{6,20}	285859.7 (0.4)	291	14.106	2.73	42.1	9.2
22 _{7,15} → 22 _{6,16}	287253.6 (0.2)	239	11.902	2.41	55.5	6.2
21 _{7,15} → 21 _{6,16}	290830.5 (0.2)	222	11.157	} 2.39 ^e	52.5	4.7
42 _{9,33} → 42 _{8,34}	290858.8 (7.8)	753	28.013			
19 _{7,13} → 19 _{6,14}	293001.6 (0.1)	192	9.733	2.69	59.5	6.4
33 _{6,28} → 33 _{5,29}	294443.0 (0.0)	452	17.672	1.68	59.5	4.0
16 _{7,9} → 16 _{6,10}	295303.4 (0.0)	153	7.651	1.59	46.7	4.8
19 _{3,17} → 18 _{2,16}	304189.9 (0.0)	147	8.886	2.08	64.1	4.6
22 _{1,21} → 21 _{2,20}	310554.7 (0.0)	180	16.308	3.39	82.4	5.8
23 _{1,23} → 22 _{0,22}	310782.7 (0.0)	182	21.124	5.03	84.3	8.5
27 _{8,20} → 27 _{7,21}	331211.8 (0.7)	346	14.862	} 3.71	48.9	8.1
26 _{8,18} → 26 _{7,19}	331240.1 (0.6)	327	14.125			
39 _{8,32} → 39 _{7,33}	331381.8 (2.5)	644	23.430	1.33	48.3	3.9
12 _{3,9} → 11 _{2,10}	331599.6 (0.0)	68	1.991	1.14	52.6	3.1
24 _{3,21} → 23 _{4,20}	336469.4 (0.1)	235	9.160	3.77	65.4	8.2
25 _{1,25} → 24 _{0,24}	337196.1 (0.1)	214	23.128	} 16.97	54.2	37.2
24 _{1,23} → 23 _{2,22}	337206.1 (0.0)	212	18.345			
16 _{8,8} → 16 _{7,9}	341875.8 (0.1)	169	7.078	1.80	81.1	3.1
12 _{4,8} → 11 _{3,9}	345580.9 (0.0)	75	3.995	1.43	53.7	3.8
24 _{2,22} → 23 _{3,21}	347788.1 (0.1)	225	14.197	4.08	69.0	8.4
35 _{5,31} → 35 _{4,32}	348661.4 (1.3)	487	14.380	1.68	65.6	3.6
26 _{0,26} → 25 _{1,25}	350399.0 (0.1)	231	24.130	8.19	71.4	16.3
25 _{2,24} → 24 _{1,23}	350707.9 (3.7)	229	19.361	6.73	70.2	13.6
SMA deblended ^f						
27 _{8,20} → 27 _{7,21}	331212.8 (0.7)	346	14.862	1.87	48.9	4.6
26 _{8,18} → 26 _{7,19}	331240.1 (0.6)	327	14.125	1.84	48.9	4.5
25 _{1,25} → 24 _{0,24}	337196.1 (0.1)	214	23.128	9.29	54.2	22.8
24 _{1,23} → 23 _{2,22}	337206.1 (0.0)	212	18.345	7.67	54.2	18.8

Notes. ^(a) Rest frequency (and its error). ^(b) Flux integrated between 0 and 62 km s⁻¹ within the full synthesized beam. ^(c) The rms per bin of 2.7 km s⁻¹ (PdBI) or 0.8 km s⁻¹ (SMA). ^(d) The signal-to-noise ratio. ^(e) Lines are not included in Fig. 7. ^(f) Parameters for the deblended lines (see Sect. 3.3).

sources which have a higher density of lines (e.g., IRC+10°216 and hot cores). Therefore, the probability that the emission features assigned to all 8 lines of TiO, or all 27 lines of TiO₂ are due to chance coincidences with lines of other species is exceedingly low in VY CMa: < 10⁻¹⁰ for TiO and < 10⁻¹⁸ for TiO₂.⁶

The velocity ranges in which the emission of TiO and TiO₂ is observed are well within those of other firmly identified molecules in VY CMa. For example, in Fig. 2 we compare the newly discovered emission to a profile of NaCl combined of many lines detected in the survey, and to the strongest emission line of SO₂ (at 283.46 GHz), all extracted for the

⁶ For TiO₂, the probability is even lower as more than 27 lines are seen. Above, we have presented only lines that are not contaminated by any other emission, while there are many examples of TiO₂ lines which interfere with emission lines of other species; the presence of TiO₂ in many such cases is evident when the blended profile is compared to a sequence of other uncontaminated profiles of the species.

same aperture 1''×1''. Lines of NaCl are among the narrowest features observed in VY CMa (Milam et al. 2007), while SO₂ shows broad, multicomponent emission typical of many sulphur-bearing species in this object. The weak emission of the two titanium oxides is located almost exactly within the velocity range of the SO₂ profile, while the main component of the TiO emission covers the same range as the NaCl profile. This correspondence is additional strong evidence in support of our identification.

4. Analysis of rotational-temperature diagrams

We made an attempt to constrain the physical conditions of the emitting gas by analysing the Boltzmann (rotational temperature) diagrams (e.g., Snyder et al. 2005) for both molecules under the assumption of LTE and optically thin emission. The rotational temperature (T_{rot}) and total column density (N) were

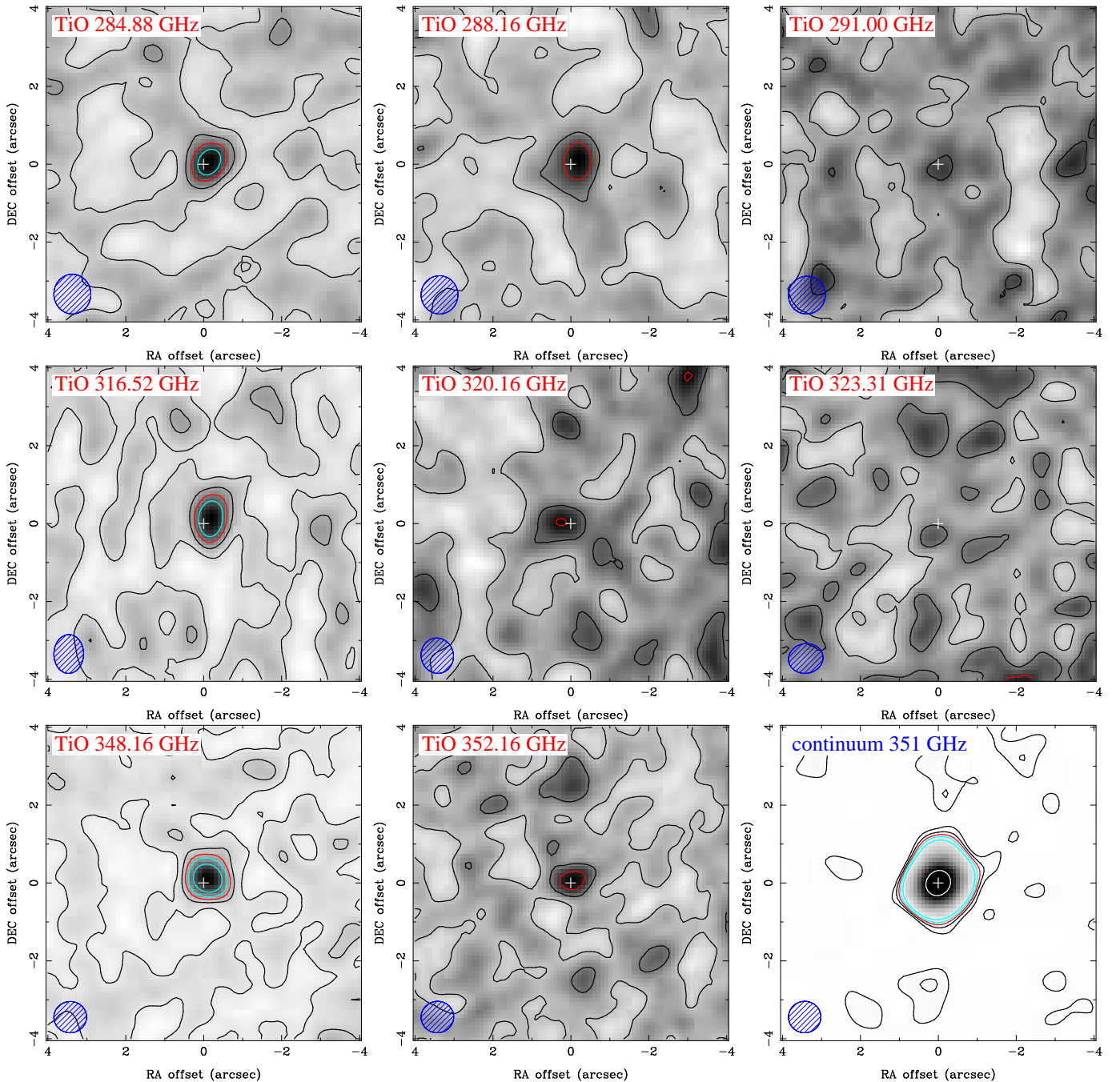


Fig. 4. All but the bottom right panel: Maps of emission integrated in the $6\text{--}36\text{ km s}^{-1}$ range for all the TiO lines covered in the SMA survey. The columns are ordered (left to right) by ${}^3\Delta_1$, ${}^3\Delta_2$, ${}^3\Delta_3$; and the rows (top to bottom) by $J = 9 \rightarrow 8$, $10 \rightarrow 9$, and $11 \rightarrow 10$. The bottom right panel: map of the continuum around 351 GHz. The beam at half power is shown in the bottom left corner of each map. The contours are drawn at 1.5σ and 3σ (black), 4.5σ (red), 6σ and 9σ (cyan), 120σ (white), where σ represents the noise levels measured in the integrated-intensity maps. The white cross (+) marks the peak of the continuum emission.

obtained from results of least-squares fits to the measurements weighed by their uncertainties. The fluxes of the PdBI data were scaled to correspond to the aperture of $1'' \times 1''$.

TiO: Shown in Fig. 6 is a rotational temperature diagram of TiO derived from measurements in Table 1. Owing to the large uncertainties in the fluxes of the eight lines because of noise and systematic effects, we were unable to constrain the rotational temperature when the line at 291.0 GHz was omitted in the analysis – i.e., the line representing the best fit parameters has a negative slope which is nonphysical under LTE conditions and inconsistent with the upper limit on the 291.0 GHz line. As men-

tioned in Sect. 3.1, the line at 291.0 GHz is close to the detection limit. When the upper limit on this emission was taken into account in the fitting procedure, we obtained $T_{\text{rot}} = 1010 \pm 870\text{ K}$ and $N(\text{TiO}) = (6.9 \pm 0.9) \cdot 10^{14}\text{ cm}^{-2}$. This solution is shown in Fig. 6 and also in Fig. 1, where Gaussian profiles are overlaid on observed lines to illustrate the relative intensity scale at the derived temperature. The quoted errors were derived from the formal uncertainties of the fit. While the rotational temperature remains poorly constrained, the uncertainty in column density is small.

The failure to constrain T_{rot} from the diagram may imply that the assumption of LTE is not valid for the TiO gas. In-

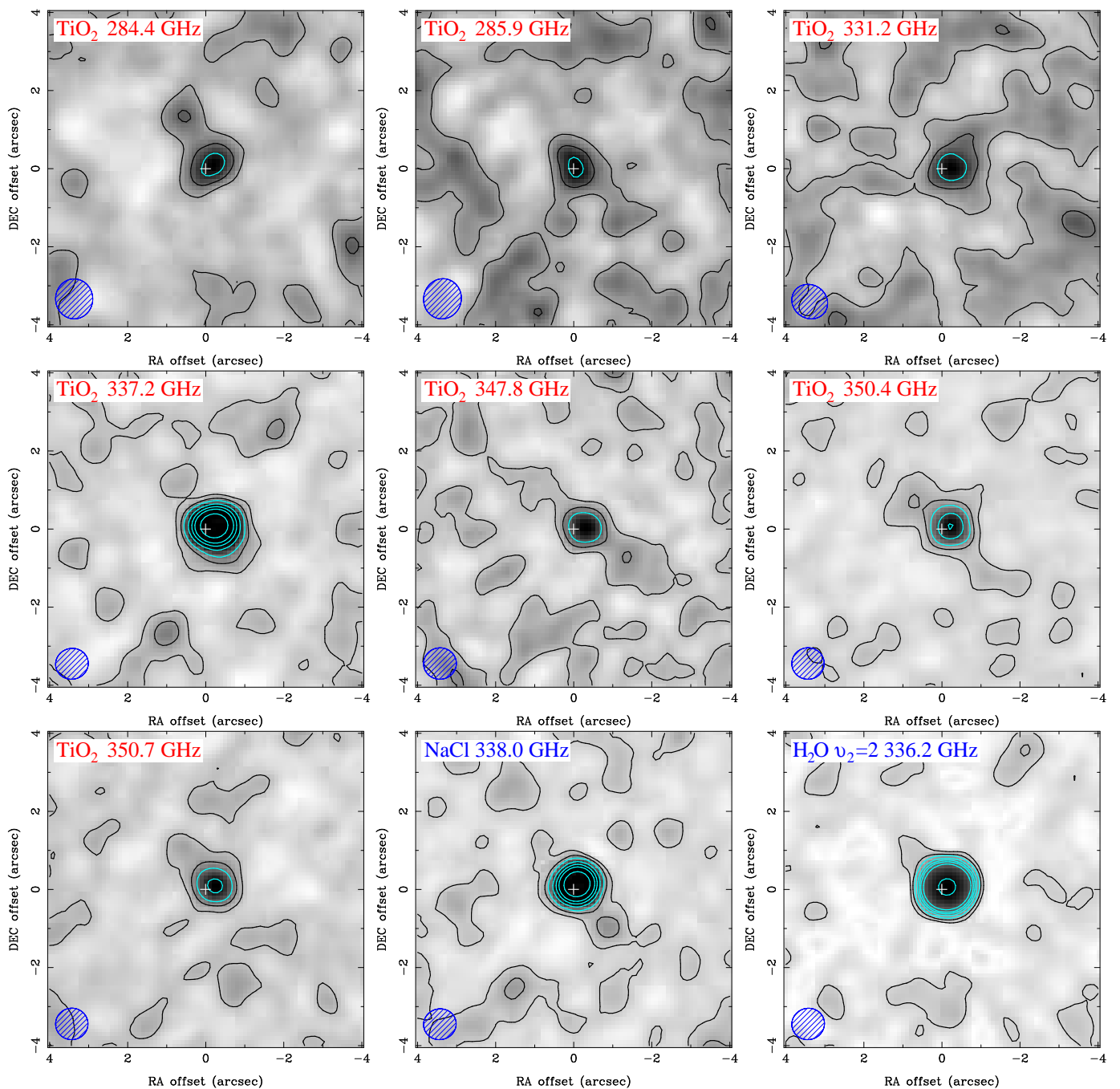


Fig. 5. The same as Fig. 4 but for the strongest emission features of TiO₂ and intensity integrated in the range 0–62 km s⁻¹ (adequately wider for blends). For comparison, emission of NaCl $J=26\rightarrow25$ and H₂O $v_2=2$ $J_{K_a,K_c}=5_{2,3}\rightarrow6_{1,6}$ is shown. The contours are at 5, 7.5 σ (black), and 10, 15, 20, 25, 35, 120 σ (cyan). See Table 2 for quantum numbers corresponding to the TiO₂ lines shown.

deed, VY CMa displays optical TiO emission whose presence implies non-LTE effects, most likely related to the strong stellar radiation (cf. Kamiński et al. 2013). Large scatter of points on a rotational temperature diagram and inability to constrain T_{rot} are problems we have encountered for several other molecules observed in the SMA survey, including NaCl and SiS for which many lines (>15) are observed, all at higher S/N. Although, optical and infrared pumping may be important in the rotational excitation of TiO, the uncertainties in the current measurements are too large to allow any conclusive statements.

TiO₂: A rotational temperature diagram of TiO₂ derived from the measurements in Table 2 is shown in Fig. 7. For those lines that are blended and arise from levels of similar energy, the

flux of the individual line was estimated from the intensity of the observed feature divided by the Einstein coefficient (A_{ul}) of each line (see the lower part of Table 2 labelled “SMA deblended”). The deblended lines are plotted in the diagram but were not included in the fit. The best fit to all detected lines (SMA and PdBI) gives $T_{\text{rot}}=255\pm24$ K and $N(\text{TiO}_2)=(7.5\pm0.9)\cdot10^{14}$ cm⁻³. This solution is also consistent with numerous 5 σ upper limits, some of which can be seen in the diagram.

Although the fit is satisfactory (the confidence level is above 99%), it corresponds to the *average* gas parameters over the entire velocity range between 0 and 62 km s⁻¹ and omits the most blue-shifted component in the PdBI spectra. The different ve-

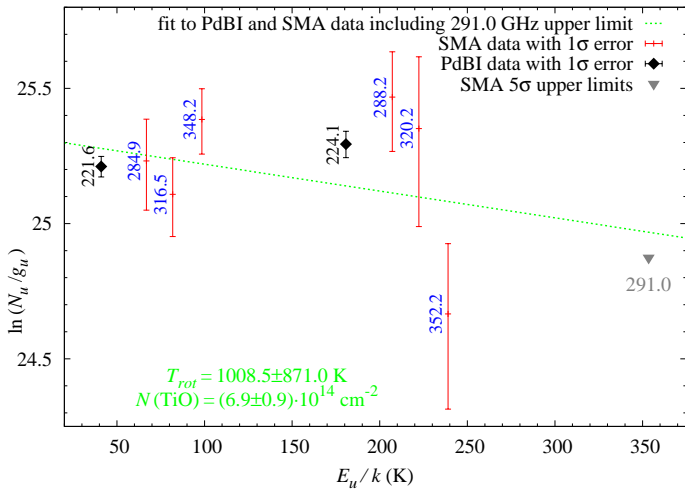


Fig. 6. Rotational temperature diagram of TiO. The upper limit on the line at 323.31 GHz is above the range on the vertical scale.

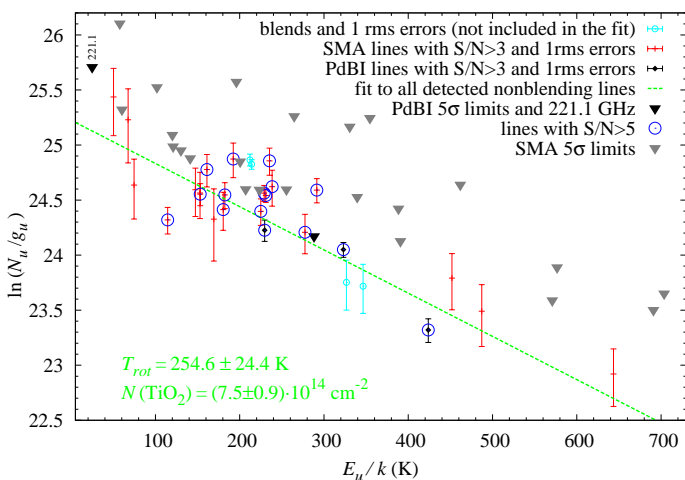


Fig. 7. Rotational temperature diagram of TiO₂.

locity components contributing to the TiO₂ emission may have different temperatures.

In the above analysis, the data from SMA and PdBI were combined despite the possibility that the molecular emission is time variable. We note, however, that temperatures calculated for PdBI and SMA data separately are consistent within uncertainties ($T_{\text{rot}}^{\text{PdBI}} = 200 \pm 60$ K and $T_{\text{rot}}^{\text{SMA}} = 305 \pm 35$ K, respectively), justifying our fit to the combined data.

5. TiO at radio and optical wavelengths

To compare the rotational profiles of TiO observed at radio and optical wavelengths, we used an optical spectrum of VY CMa obtained in 2001 with the Very Large Telescope (VLT) and reported in Kamiński et al. (2013). Referring to the TiO line list of G. J. Phillips⁷, we searched for single-component and well separated rotational lines, and chose two examples in the γ (0,0) band. A line at the rest wavelength $\lambda_{\text{lab}} = 7076.93 \text{ \AA}$ is mainly formed by the $Q_3(J=34)$ transition and is affected by the presence of components from higher vibrational bands (at 9 km s^{-1} with respect to λ_{lab}); moreover, the wings of the line are blended with those of other nearby rotational lines. Another line, at $\lambda_{\text{lab}} = 7082.64 \text{ \AA}$, is formed mainly by $P_3(26)$ and $Q_3(39)$ (and

$R_1(118)$ of the (4,3) band) and is much better separated from the neighboring rotational components; its red wing, however, has some contribution from the weak $R_3(59)$ line (at 7 km s^{-1} with respect to the main components). The structure of the lines is illustrated in Fig. 8, where the profiles are also compared to the combined SMA profile.

The profile of the optical and radio emission is very similar. The optical lines are however slightly narrower than the combined SMA profile if results of Gaussian fits performed within $3\text{--}32 \text{ km s}^{-1}$ are compared; the average FWHM of the two optical lines shown in Fig. 8 is $12 \pm 3 \text{ km s}^{-1}$. Some other rotational lines measured are as narrow as 9 km s^{-1} FWHM, but due to unknown level of the photospheric fluxes these widths may be underestimated. For the same reason, the presence of the broad pedestal seen in the radio spectra cannot be investigated. The peaks of the optical lines are at $V_{\text{LSR}} = 22 \pm 1 \text{ km s}^{-1}$ and there is no systematic shift of line centers with J . Taking into account the uncertainty in the wavelength calibration of $3 \text{ rms} = 0.7 \text{ km s}^{-1}$, this peak velocity is formally consistent with the location of the center of the combined SMA profile ($V_{\text{LSR}} = 20 \pm 2 \text{ km s}^{-1}$). Similarly, Wallerstein (1986) derived $V_{\text{LSR}} = 24 \pm 2 \text{ km s}^{-1}$ from positions of the TiO band heads, which to within the errors is consistent with the peak position of the radio emission. However, when the profiles are overplotted, the optical lines appear to be systematically shifted by about 2 km s^{-1} with respect to the radio profile (note that a compensating correction was applied in Fig. 8). Some red-shift of the optical emission with respect to the radio emission is expected owing to scattering of the optical radiation on grains within the dusty nebula (van Blerkom & van Blerkom 1978; Humphreys et al. 2005). As noted in Kamiński et al. (2013), this red-shift of optical lines must be less than about 3 km s^{-1} and does not affect considerably the profiles for the line of sight towards the star; both effects are significant only in the outer parts of the nebula (Humphreys et al. 2005).

Rotational temperatures derived from our measurements of the pure rotational spectrum and previous optical studies of TiO are consistent, although the uncertainties are high in both. Phillips & Davis (1987) derived a rotational temperature of 600 K with an uncertainty of about 150 K from the rotational structure of the γ' system at 6200 \AA ($B^3\Pi-X^3\Delta$), however there are two possible sources of systematic error in the optical measurements. First, the analysis of Phillips & Davis (1987) requires a revision with a new TiO line list containing improved oscillator strengths (e.g., Schwenke 1998). The new data can change the shape and intensity of the simulated spectrum of the emission (and the underlying photospheric absorption), thus yielding revised estimates of the rotational temperature (Allard et al. 2000). Second, because the optical emission spectrum of VY CMa and the bands of TiO are time variable (e.g., Wallerstein 1986), the excitation temperature of TiO may be time variable too. For example, rotational temperatures derived from the orange (0,0) band of the $A^2\Pi-X^2\Sigma$ system of ScO differed by more than a factor of two on two different dates ($T_{\text{rot}} = 380 \text{ K}$ and 820 K in 1962 and 1966, respectively; Herbig 1974).

The above comparison provides further strong evidence in support our identification of TiO radio emission. The similarity of the optical profiles and the main (central) component of the (sub-)millimeter emission suggests that they arise in the same circumstellar gas.

⁷ available on the web site of R. L. Kurucz <http://kurucz.harvard.edu>

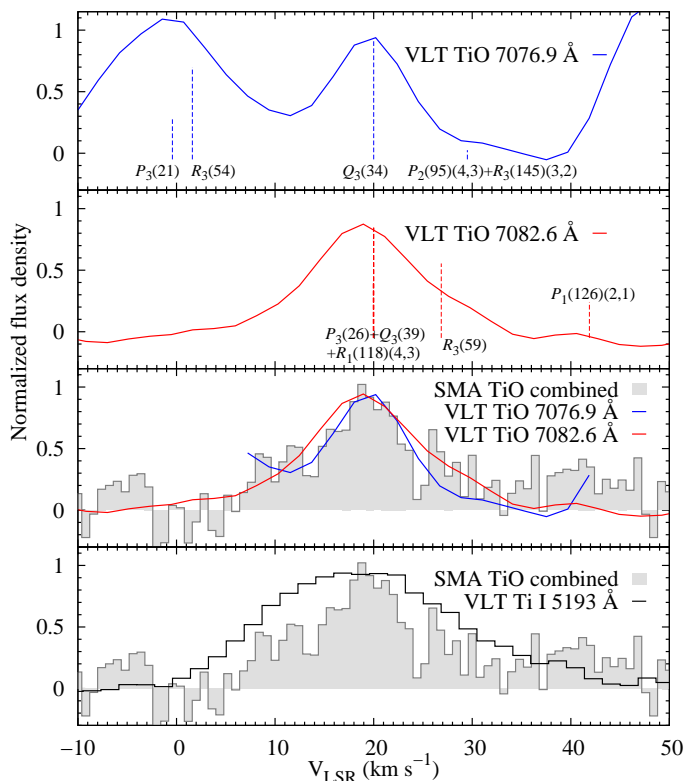


Fig. 8. Rotational profiles of TiO emission in the γ system near 7080 Å (panels first and second from the top) are compared to the combined SMA profile of TiO (third panel from the top). Bottom panel: the Ti I line at 5193 Å is overlaid on the combined SMA profile. The vertical lines mark positions of rotational components of the (0,0) band, unless otherwise indicated in the labels in the Figure. All the optical lines were shifted arbitrarily by -2 km s^{-1} to facilitate direct comparison with the SMA radio profile.

6. Discussion

6.1. Localization and abundances of the TiO and TiO₂ gas

The displacement of the center of the molecular emission with respect to continuum peak (Sect. 3.6) brings into question the actual position of the star in our self-calibrated maps. The continuum source is resolved in the SMA observations at a very high S/N (~ 200 for the peak flux in a single 2 GHz-band) and is elliptical in shape with $0''.5 \times 0''.3$ FWHM. Therefore the origin of the radio continuum is certainly not entirely photospheric. Indeed, models of the spectral energy distribution of VY CMa (e.g., Harwit et al. 2001) suggest that at the observed frequencies the total flux is almost entirely reprocessed dust radiation, with the direct photospheric flux constituting only a few percent of the total emission. Our measured flux of 0.6 Jy at 320 GHz is consistent with those models. Although both dust and molecular gas are likely to have a very inhomogeneous distribution around VY CMa even at lowest spatial scales, we believe it is the center of molecular emission that can be identified as the position of the star itself. In support to this interpretation comes the observation that emission of transitions from highly excited states, like that of H₂O $v_2=2$ $J_{K_a, K_c}=5_{2,3} \rightarrow 6_{1,6}$ with $E_u=2955 \text{ K}$, peaks at this location; since it requires a nearby energetic excitation source, e.g., energetic radiation or high-density gas of high temperature, it is very likely located close to the star. Additionally, to produce centrally peaked profiles (like those of TiO and NaCl) and emission center displaced with respect to the kinematical center,

the gas would have to move tangentially with almost no radial component, which is very unlikely in this source. Moreover, Muller et al. (2007) noticed a very similar spatial shift between the centroid of the continuum emission at 1.3 mm and the positions of the masers of SiO, H₂O, and OH in VY CMa. The positional shift between the continuum and molecular emission will be discussed in more detail in a separate paper. In the following discussion we assume the observed molecular emission is spatially centered on the star.

That the TiO₂ emission reaches the outflow terminal velocity ($V_\infty=40\text{--}45 \text{ km s}^{-1}$, Humphreys et al. 2005) implies that at least part of the outflow is already accelerated to V_∞ . In case of TiO, the broad pedestal can be traced to high expansion velocities but due to a very low S/N it is uncertain whether it indeed reaches V_∞ (Fig. 2). The main Gaussian-like component of the TiO emission, however, is very likely formed in the inner outflow because it is centrally peaked and much narrower than $2V_\infty$. Similar narrow molecular emission lines in VY CMa have been attributed to the accelerating wind (e.g., Milam et al. 2007). Following Tenenbaum & Ziurys (2009) and Kamiński et al. (2013), to better localize the TiO emission region we use the semi-empirical wind-acceleration model in VY CMa constrained from multi-epoch observations of H₂O masers (Richards et al. 1998). This model assumes linear wind acceleration within 75–440 mas from the star and does not take into account the inhomogeneities of the wind at these scales. Ignoring the weak pedestal, the main TiO component has a full width of about $40 \pm 5 \text{ km s}^{-1}$, implying that the emission region extends out to $r=28 \pm 10 R_\star$ ($R_\star=2000 R_\odot$) or $0''.18 \pm 0''.07$ at 1.2 kpc and the emission corresponding to the broad pedestal is located at even larger distances from the star.

With the average deconvolved size of the of TiO₂ emission of $\text{FWHM}=0''.6$, more than 99% of the flux is enclosed within a region of the radius of $r=3\sigma/2=3\sqrt{2} \ln 2 \text{ FWHM}=0''.4$ or $r=50(\pm 10) R_\star$. Using this value and the size of $r=28 R_\star$ for TiO, we can correct the column densities derived in Sect. 4 for the corresponding beam filling factors. In this way, we obtain $N(\text{TiO})=(6.7 \pm 0.8) \cdot 10^{15} \text{ cm}^{-2}$ and $N(\text{TiO}_2)=(1.8 \pm 0.2) \cdot 10^{15} \text{ cm}^{-2}$. For a mass-loss rate of $10^{-4} M_\odot \text{ yr}^{-1}$ (Danchi et al. 1994) and an average expansion velocity of 10 km s^{-1} for TiO and 20 km s^{-1} for TiO₂, the molecular abundances with respect to the column of hydrogen (assumed to be in molecular form only) are $[f_1]=\log(N_{\text{TiO}}/N_{\text{H}})=-8.6$ and $[f_2]=\log(N_{\text{TiO}_2}/N_{\text{H}})=-9.5$, but these estimates are very approximate.

6.2. Ti oxides and the formation of inorganic dust

Our interferometric observations of TiO and TiO₂ allow us to critically examine present ideas about the onset of nucleation and the formation of inorganic dust in oxygen-rich objects with high mass-loss rates. In the chemical equilibrium model of Gail & Sedlmayr (1998), TiO exists in the photospheres of cool stars because the bond dissociation energy is high. As a result it is observed in regions with effective temperatures $T_{\text{eff}} \lesssim 4000 \text{ K}$ as well as in the cooler material just above the photosphere. TiO₂ is predicted to form in the reaction of TiO with H₂O which is abundant in these environments (Royer et al. 2010). Owing to the lower bond dissociation energy of TiO₂, it is predicted to be more abundant than TiO only at lower temperatures. At temperatures above about 1400 K, TiO is the dominant carrier of gas phase titanium; below this temperature TiO₂ is the most abundant carrier of titanium; and at 1100 K only about 10% of all titanium-bearing molecules are TiO. At slightly lower tempera-

tures, TiO₂ nucleates to produce larger oxides and their clusters thereby initiating the formation of dust “seeds”.

Dust formation in VY CMa occurs at a radius⁸ of 0′′05–0′′12, or 6–15 R_★ (Monnier et al. 2000; Le Sidaner & Le Bertre 1996). The prediction of Gail & Sedlmayr (1998) that TiO should be located primarily inside the dust formation zone is inconsistent with our estimate that the size of the TiO emission region of 28 R_★. Unfortunately, our estimate of the rotational temperature ($T_{\text{rot}}=1010\pm 870$ K, Sect. 3.1) is too uncertain to test the prediction of Gail & Sedlmayr that $T \geq 1100$ K, but the relatively large observed line widths of TiO are inconsistent with the model. Although it is plausible that the outflow traced by the TiO gas is already accelerated to large velocities below the dust formation region⁹, it is more likely that the TiO emission does not originate from inside the dust formation zone, but rather from a much more extended region. Similarly, the model of Gail & Sedlmayr (1998) is in poor agreement with the observed properties of TiO₂. The temperature derived from the observations is about 250 K, but is predicted to be about 4–5 times higher. The TiO₂ emission comes from a region ($r \approx 0′′4$), that is a few times larger than the size predicted for the dust formation region, although the uncertainties in both are quite large. Moreover, the offset of the peak emission for both molecules with respect to the center of continuum source cannot be easily reconciled with the predictions.

Inconsistencies are also encountered when the observations are referred to the equilibrium-chemistry model of Sharp & Huebner (1990). In their model which includes condensation, emission of TiO or TiO₂ only arises from the warm gas ($T \geq 1400$ K) located in a thin layer above the photosphere. Simple equilibrium-chemistry models evidently cannot explain the observations of VY CMa. Indeed, molecular abundances calculated for molecular equilibrium have been demonstrated to fail observational tests in AGB stars (Cherchneff 2006) and for some species in VY CMa (Tenenbaum & Ziurys 2009; Kamiński et al. 2013). A non-equilibrium approach is needed to explain the circumstellar chemistry of supergiants but such models do not exist.

Absorption bands of TiO are common features in optical spectra of cool photospheres. Although emission bands of TiO are rarely observed, they are present in VY CMa, and very rich TiO emission is seen in the spectra of U Equ and V4332 Sgr (Barnbaum et al. 1996; Kamiński et al. 2010) — two peculiar stars thought to have recently experienced a major cataclysm (a planet-engulfment and a stellar merger, respectively; Geballe et al. 2005; Tylenda & Soker 2006). Emission of TiO was also identified in several B[e] supergiants (Zickgraf et al. 1989) and a few protostars (Hillenbrand et al. 2012), including some that are known to be explosive objects. Recently, an emission feature of TiO was discovered in the IR (around 10 μm) in four S-type Mira variables which are large-amplitude pulsators (Smolders et al. 2012). A common property of these objects (including VY CMa) is the relatively violent environment in which the TiO emission is observed. In VY CMa, it has been suggested that the outflow was formed by episodic events of enhanced mass loss or “localized mass ejections” (Smith et al.

⁸ The dust formation radius is poorly defined owing to the asymmetry and probable variability of the star. Its location derived from observations depends on the stellar parameters and dust type that were assumed, explaining in part the broad range of values cited in the literature.

⁹ Outflows in luminous cool stars may be driven by radiation pressure absorbed in molecular bands as proposed by Jorgensen & Johnson (1992, and references therein), or the mass loss might be driven by the convective/magnetic activity of the giant star (e.g., Smith et al. 2001) which may lead to considerable turbulent motions very close to the star.

2001; Humphreys et al. 2007) most likely involving shocks (cf. Kamiński et al. 2013). If newly formed dust is destroyed close to the star by shocks, it might give rise to molecular emission at temperatures below ~1100 K. The observed variability of the optical TiO bands also suggests that the emission is linked to the stellar activity.

However the kinematic separation of TiO and TiO₂ implied by the line profiles in Fig. 2 (i.e., TiO emission is highest at velocities where the TiO₂ emission has local minima) would appear to contradict this interpretation — one might expect that simple destruction of the dust would release TiO and TiO₂ at the same location. A plausible explanation which is consistent with the observations is that when violent shocks release TiO, the TiO₂ is destroyed but it reforms when water reacts with TiO farther from the star.

Another possible explanation for the Ti oxides we observe is incomplete formation of the dust. The extended reflection nebula confirms that dust has been effectively formed in VY CMa for the last 1000 yr or more (e.g., Humphreys et al. 2007), but owing to the high mass-loss rate ($\sim 10^{-4} M_{\odot} \text{ yr}^{-1}$) a sufficient fraction of TiO and TiO₂ might survive the nucleation process to account for the observed abundances in the cooler region. The apparent stratification of TiO and TiO₂ that we observe might then be understood within the context of the model of Gail & Sedlmayr (1998). In addition, equilibrium-chemistry models of Sharp & Huebner (1990) show that the titanium oxides remain relatively abundant throughout the outflow if no condensation takes place. VY CMa may be an intermediate case between full versus no condensation.

All of the models referred to here predict that titanium is converted to the oxides in the inner outflow, but emission features of atomic Ti are observed in the visible at the systemic velocity (Wallerstein 1986; Wallerstein & Gonzalez 2001). By examining a pure emission feature of Ti I at 5193 Å in the VLT spectrum, we find that it covers the range from 0 to 45 km s⁻¹, i.e., is slightly broader than the central component of the radio TiO emission (see Fig. 8). This implies that gas-phase Ti I extends farther from the star than the gas with highest TiO abundance. It has long been known that atomic Ti is highly depleted in the diffuse interstellar medium (e.g., Stokes 1978), implying that Ti either forms molecules and remains in the gas phase, or it is effectively locked into dust. The observed optical emission of Ti is further evidence that the condensation of Ti species in VY CMa is not as efficient as previously estimated, or that the Ti species extend to much larger radii than commonly assumed. Any future attempts to explain this anomaly should take into account those optical observations of atomic titanium. At this moment the observational characteristics of Ti-bearing species in VY CMa remain unexplained.

6.3. Prospects

The detection of TiO and TiO₂ in the cooler region of the CSE of an oxygen-rich late-type star, implies that other small transition-metal bearing molecules such as VO, ScO, YO, and CrO might be found with sensitive interferometers in the (sub-)millimeter wave band. Observations of TiO and TiO₂ with the Atacama Large Millimeter Array (ALMA) when the full sensitivity and angular resolution is attained, should resolve the region where they are present and establish whether there is evidence for stratification between species. This in turn would allow more detailed studies of titanium depletion to oxides and solids.

Acknowledgements. HSPM thanks the Bundesministerium für Bildung und Forschung (BMBF) for support via project FKZ 500F0901 (ICC HIFI *Herschel*). The Submillimeter Array is a joint project between the Smithsonian Astrophysical Observatory and the Academia Sinica Institute of Astronomy and Astrophysics and is funded by the Smithsonian Institution and the Academia Sinica. IRAM is supported by INSU/CNRS (France), MPG (Germany) and IGN (Spain). We acknowledge these institutions.

References

- Allard, F., Hauschildt, P. H., & Schwenke, D. 2000, *ApJ*, 540, 1005
 Barnbaum, C., Omont, A., & Morris, M. 1996, *A&A*, 310, 259
 Brünken, S., Müller, H. S. P., Menten, K. M., McCarthy, M. C., & Thaddeus, P. 2008, *ApJ*, 676, 1367
 Cherchneff, I. 2006, *A&A*, 456, 1001
 Churchwell, E., Hocking, W. H., Merer, A. J., & Gerry, M. C. L. 1980, *AJ*, 85, 1382
 Danchi, W. C., Bester, M., Degiacomi, C. G., Greenhill, L. J., & Townes, C. H. 1994, *AJ*, 107, 1469
 Fu, R. R., Moullet, A., Patel, N. A., et al. 2012, *ApJ*, 746, 42
 Gail, H.-P., & Sedlmayr, E. 1998, *Faraday Discussions*, 109, 303
 Geballe, T. R., Barnbaum, C., Noll, K. S., & Morris, M. 2005, *ApJ*, 624, 983
 Harwit, M., Malfait, K., Decin, L., et al. 2001, *ApJ*, 557, 844
 Herbig, G. H. 1974, *ApJ*, 188, 533
 Hillenbrand, L. A., Knapp, G. R., Padgett, D. L., Rebull, L. M., & McGehee, P. M. 2012, *AJ*, 143, 37
 Humphreys, R. M., Davidson, K., Ruch, G., & Wallerstein, G. 2005, *AJ*, 129, 492
 Humphreys, R. M., Helton, L. A., & Jones, T. J. 2007, *AJ*, 133, 2716
 Jeong, K. S., Winters, J. M., Le Bertre, T., & Sedlmayr, E. 2003, *A&A*, 407, 191
 Jorgensen, U. G., & Johnson, H. R. 1992, *A&A*, 265, 168
 Kamiński, T., Schmidt, M., & Tylenda, R. 2010, *A&A*, 522, A75
 Kamiński, T., Schmidt, M., & Menten, K. M. 2013, *A&A*, 549, A6
 Kania, P., Hermanns, M., Brünken, S., Müller, H. S. P., & Giesen, T. F. 2011, *J. Mol. Spectrosc.*, 268, 173
 Le Sidaner, P., & Le Bertre, T. 1996, *A&A*, 314, 896
 Menten, K. M., Philipp, S. D., Güsten, R., et al. 2006, *A&A*, 454, L107
 Merrill, P. W., Deutsch, A. J., & Keenan, P. C. 1962, *ApJ*, 136, 21
 Milam, S. N., Apponi, A. J., Woolf, N. J., & Ziurys, L. M. 2007, *ApJ*, 668, L131
 Millar, T. J., Ellender, J., Hjalmarson, A., & Olofsson, H. 1987, *A&A*, 182, 143
 Monnier, J. D., Danchi, W. C., Hale, D. S., Tuthill, P. G., & Townes, C. H. 2000, *ApJ*, 543, 868
 Morgan, W. W., & Keenan, P. C. 1973, *ARA&A*, 11, 29
 Muller, S., Dinh-V-Trung, Lim, J., et al. 2007, *ApJ*, 656, 1109
 Müller, H. S. P., Schlöder, F., Stutzki, J., & Winnewisser, G. 2005, *J. Mol. Struct.*, 742, 215
 Müller, H. S. P., Thorwirth, S., Roth, D. A., & Winnewisser, G. 2001, *A&A*, 370, L49
 Namiki, K.-I., Saito, S., Robinson, J. C., & Steimle, T. C. 1988, *J. Mol. Spectrosc.*, 191, 176
 Phillips, J. G., & Davis, S. P. 1987, *PASP*, 99, 839
 Pickett, H. M., Poynter, R. L., Cohen, E. A., et al. 1998, *J. Quant. Spec. Radiat. Transf.*, 60, 883
 Reid, M. J., & Goldston, J. E. 2002, *ApJ*, 568, 931
 Richards, A. M. S., Yates, J. A., & Cohen, R. J. 1998, *MNRAS*, 299, 319
 Royer, P., Decin, L., Wesson, R., et al. 2010, *A&A*, 518, L145
 Sault, R. J., Teuben, P. J., & Wright, M. C. H. 1995, *Astronomical Data Analysis Software and Systems IV*, 77, 433
 Schwenke, D. W. 1998, *Faraday Discussions*, 109, 321
 Sedlmayr, E., & Dominik, C. 1995, *Space Sci. Rev.*, 73, 211
 Sharp, C. M., & Huebner, W. F. 1990, *ApJS*, 72, 417
 Smith, N., Humphreys, R. M., Davidson, K., et al. 2001, *AJ*, 121, 1111
 Smolders, K., Verhoelst, T., Neykens, P., et al. 2012, *A&A*, 543, L2
 Snyder, L. E., Lovas, F. J., Hollis, J. M., et al. 2005, *ApJ*, 619, 914
 Steimle, T. C., & Virgo, W. 2003, *Chem. Phys. Lett.*, 381, 30
 Stokes, G. M. 1978, *ApJS*, 36, 115
 Tenenbaum, E. D., Dodd, J. L., Milam, S. N., Woolf, N. J., & Ziurys, L. M. 2010, *ApJS*, 190, 348
 Tenenbaum, E. D., & Ziurys, L. M. 2009, *ApJ*, 694, L59
 Tylenda, R., & Soker, N. 2006, *A&A*, 451, 223
 van Blerkom, J., & van Blerkom, D. 1978, *ApJ*, 225, 482
 Wallerstein, G. 1986, *A&A*, 164, 101
 Wallerstein, G., & Gonzalez, G. 2001, *PASP*, 113, 954
 Wang, H., Steimle, T. C., Apetrei, C., Maier, J. P. 2009, *Phys. Chem. Chem. Phys.*, 11, 2649
 Wittkowski, M., Hauschildt, P. H., Arroyo-Torres, B., & Marcaide, J. M. 2012, *A&A*, 540, L12
 Zhang, B., Reid, M. J., Menten, K. M., & Zheng, X. W. 2012, *ApJ*, 744, 23
 Zickgraf, F.-J., Wolf, B., Stahl, O., & Humphreys, R. M. 1989, *A&A*, 220, 206
 Ziurys, L. M., Milam, S. N., Apponi, A. J., & Woolf, N. J. 2007, *Nature*, 447, 1094

Table A.1. Lines identified in the PdBI spectrum.

Mole- cule	Transition ^a	ν_{rest} (GHz)	E_u (K)	S_{ul} ^b	V_{cen} ^c (km s ⁻¹)
TiO ₂	23 _{5,19} → 23 _{4,20}	220.812	230	12.857	14.8
TiO ₂	4 _{4,0} → 3 _{3,1}	221.096	25	3.476	17.1
³⁴ SO ₂	22 _{2,20} → 22 _{1,21}	221.115	248	12.663	-8.9
NaCl	$J=17 \rightarrow 16$	221.260	96	14.200	21.7
KCl	$v=1, J=29 \rightarrow 28$	221.298	395	16.800	18.3
TiO ₂	32 _{5,27} → 32 _{4,28}	221.407	424	19.365	35.2
TiO ₂	28 _{4,24} → 28 _{3,25}	221.458	323	14.873	26.9
TiO	$J=7 \rightarrow 6, \Omega=1$	221.580	41	13.710	20.5
³⁴ SO ₂	13 _{2,12} → 13 _{1,13}	221.736	93	4.887	19.4
SO ₂	11 _{1,11} → 10 _{0,10}	221.965	60	7.711	24.7
(SO ₂)	$v_2=1, 11_{1,11} \rightarrow 10_{0,10}$	222.424	821	7.949	23.0
KCl	$J=29 \rightarrow 28$	222.666	116	25.000	22.4
SO ₂	27 _{8,20} → 28 _{7,21}	223.435	504	3.701	9.9
SO ₂	6 _{4,2} → 7 _{3,5}	223.883	59	0.433	35.0
TiO	$J=7 \rightarrow 6, \Omega=2$	224.139	181	12.854	21.4
SO ₂	20 _{2,18} → 19 _{3,17}	224.265	208	4.615	...

Notes. ^(a) Quantum numbers characterizing the transition in the standard notation. ^(b) The quantum mechanical line strength of the rotational transition. ^(c) Centroid position of the emission with respect to the rest frequency.

Appendix A: The PdBI spectrum of VY CMa

A spectrum extracted from the central pixel of the PdBI data is displayed in Fig. A.1.¹⁰ The line identification for this spectrum was based mainly on the results of the SMA survey, but also on some archival SMA data (e.g., Fu et al. 2012) and that of Tenenbaum et al. (2010) were consulted. The identified lines are shown in Fig. A.1 and listed in Table A.1. In addition to the targeted TiO and TiO₂ lines, the spectrum covers emission features of SO₂, ³⁴SO₂, NaCl, and KCl. Among these, KCl had not been reported in VY CMa before (a full analysis of its emission will be presented elsewhere). Near 222.45 GHz, emission and absorption features that seem to compose a P-Cyg profile are seen. The emission peak can be tentatively identified with vibrationally excited SO₂ at $v_2=1$, but the absorption occurs where two subunits of the WideX correlator are connected and is likely a spurious feature.

¹⁰ The spectrum will be also available in electronic form at the CDS via anonymous ftp to cdsarc.u-strasbg.fr (130.79.128.5) or via <http://cdsweb.u-strasbg.fr/cgi-bin/qcat?J/A+A/?????>.

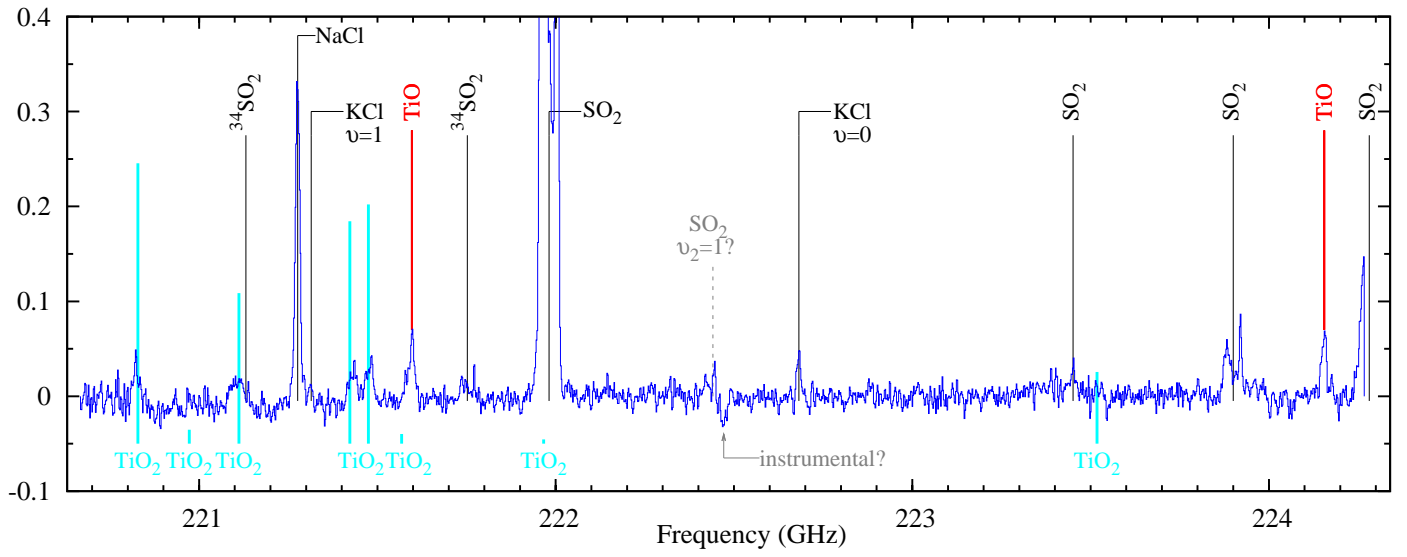


Fig. A.1. The spectrum obtained with PdBI and corresponding to the central pixel of $0'65 \times 0'65$. The continuum was subtracted. The height of the lines marking TiO_2 positions (cyan), corresponds to the *relative* intensities for LTE at 300 K. The ordinate is flux density in Jy/beam.